Aqueous-phase effects on ethanol decomposition over Ru-based catalysts

Journal:	*Catalysis Science & Technology*
Manuscript ID	CY-ART-06-2021-001057.R1
Article Type:	Paper
Date Submitted by the Author:	01-Sep-2021
Complete List of Authors:	Zare, Mehdi; University of South Carolina Saleheen, Mohammad; University of South Carolina, Chemical Engineering; Mr. Mamun, Osman; University of South Carolina, Chemical Engineering Heyden, Andreas; University of South Carolina, Chemical Engineering

Aqueous-phase effects on ethanol decomposition over Ru-based catalysts

Mehdi Zare[a], Mohammad Saleheen[a], Osman Mamun, and Andreas Heyden*

Department of Chemical Engineering, University of South Carolina, 301 Main Street, Columbia,
South Carolina 29208, USA

*Corresponding author: email: heyden@cec.sc.edu

---

[a] These authors contributed equally to this work.

Abstract

The effects of an aqueous phase on the ethanol decomposition for hydrogen production over a Ru(0001) catalyst surface model have been investigated from first principles. Solvent effects on the reaction mechanism and kinetic parameters have been quantified with the help of a microkinetic reactor model, density functional theory, and an implicit solvation scheme (*iSMS*). Our calculations indicate that in both vapor- and aqueous-phase reaction environments, the ethanol decomposition starts with acetaldehyde formation on the surface, some of which further dehydrogenates to ketenyl species (CHCO), where the C-C bond cleaves to form methylidyne (CH) and CO. In the vapor phase, adsorbed CH gets hydrogenated to methane, and CO desorbs or undergoes methanation reducing the amount of hydrogen produced. In contrast, under aqueous phase reaction conditions, the methanation is inhibited, and the water-gas shift (WGS) reaction is accelerated, leading to complete conversion of CO to CO_2 and H_2. Calculations indicate that the observed reaction behavior under aqueous phase reforming conditions originates primarily from the higher water chemical potential, and implicit solvent models predict only a small solvation effect.

1. Introduction

Fossil fuels provide a significant portion, approximately 80%, of the present world energy demand.[1] Hydrogen is regarded as a promising substitute for fossil fuels in many applications since not only does it burn cleanly, it is also abundant in the universe and has the highest energy content per unit of weight (i.e., 120.7 kJ/g) relative to any known fossil fuels.[2] Biomass-derived resources are possible candidates for hydrogen production, in particular for *in situ* hydrogen production for upgrading other biomass fractions to higher-value chemicals in a future biorefinery.[3-5] Conversion of biomass to hydrogen is a two-step process: an extraction step to produce an aqueous-phase carbohydrate bio-oil, followed by catalytic reforming of the bio-oil to produce hydrogen.[6, 7] Hydrogen production from carbohydrates such as sugars, methanol, ethanol, and polyols (e.g., ethylene glycol, glycerol) can be effectively performed in an aqueous phase at temperatures near 500 K.[8, 9]

In particular, catalytic conversion of ethanol to hydrogen has been proposed, which can be performed by either steam reforming (SR)[3, 10] or aqueous-phase reforming (APR).[11-15] Conversion of ethanol to hydrogen in an aqueous phase has several advantages over steam reforming[8, 16]: 1) APR can facilitate the Water-Gas Shift (WGS) reaction to produce more hydrogen and less CO since its operating condition is favorable for the WGS reaction, 2) APR reduces the energy cost associated with vaporization of the reactant in the SR process, 3) APR occurs at low temperature that minimizes production of undesirable components such as light hydrocarbons and CO, and 4) unlike the multi-reactor process required in SR, APR may be achieved in a single step, low-temperature process.

Ferrin et al.[17] studied ethanol decomposition on transition metals in the vapor phase at 523 K using a combination of reactor studies and computational Brønsted−Evans−Polanyi (BEP) and scaling relations. Their reported data suggest a high activity of a Ru catalyst for C-C bond cleavage in ethanol which is favorable for hydrogen production. They report a zero activity for a Cu catalyst and found Pt to be the second-best catalyst in C-C bond cleavage (Ru > Pt > Rh > Pd > Ir). In another study, Alcala et al.[9] utilized periodic density functional theory to identify the most favorable pathways for C-O and C-C bond cleavages of oxygenated hydrocarbons over a Pt(111) model surface. They found that at T > 550 K, the C-C bond cleavage is faster than the C-O bond cleavage in ethanol. Furthermore, in three independent experimental studies, Nozawa et al.,[16] Waheed et al.,[18] and Zhao et al.[19] examined the dependence of Ru particle size on activity and selectivity of the APR of ethanol over a Ru/TiO_2 catalyst at 473 K. Overall, they observed that during aqueous-phase ethanol decomposition, a catalyst with small Ru catalyst particles yields a higher H_2 efficiency since the methanation reaction is suppressed relative to larger Ru catalyst particles. To compare the catalytic activity of the different metals for C-C bond cleavage, Sinfelt and Yates[20] have studied ethane hydrogenolysis and found Ru, Ni, and Ir to be the most active metals for C-C bond breaking. However, an effective catalyst for APR is needed to be not only active but also selective. Specifically, in ethanol decomposition for hydrogen production, an excellent catalyst is required to have three main characteristics: 1) activity for C-C bond cleavage, 2) activity for the WGS reaction to convert CO and H_2O to CO_2 and hydrogen, and 3) inactivity for the methanation reaction such that few light hydrocarbons are produced. In this respect, Grenoble et al.[21] found Ru, Pt, Cu, and Ni to be good candidates for the WGS reaction. However, regarding the methanation reaction, Vannice[22] reported that Ru, Ni, and Rh exhibit a high rate for methanation. Thus, given the high C-C cleavage activity of Ru catalysts, Ru appears to be a good catalyst for hydrogen production from ethanol decomposition if the methanation reaction could be suppressed by, e.g., operation in an aqueous-phase reaction environment.

In this study, we have investigated a comprehensive reaction network consisting of 133 elementary reactions for the ethanol decomposition over a Ru(0001) catalyst surface model in both vapor and aqueous phase reaction environments using first principle DFT calculations. Having computed activation and reaction free energies for various elementary reactions, we developed a mean-field microkinetic reactor model to predict the reaction kinetics such as turnover frequency, abundant surface species, reaction orders, and apparent activation barriers in vapor and aqueous phase reaction environments. Thus, we can quantify solvation effects and understand rate and performance-limiting steps in various environments; information that is needed to further optimize Ru catalysts for hydrogen production from alcohols.

2. Methods

2.1. DFT calculations

We have performed periodic DFT calculations using the Vienna Ab Initio Simulation Package (VASP).[23, 24] A frozen-core, all-electron projector augmented-wave (PAW) method is utilized to describe the ionic core potentials.[25, 26] The surface Brillouin zone is sampled with 4 × 4 × 1 Monkhorst-Pack *k*-point mesh using Methfessel-Paxton smearing[27] ($\sigma = 0.1$ eV). The Kohn−Sham one-electron valence states are expanded in a basis of plane waves with kinetic energies below 400 eV. The self-consistent field (SCF) is converged to 1.0×10^{-7} eV and a force-based criterion of 0.01 eV/Å is used for the ionic cycle convergence. The PBE functional form, Perdew, Burke, and Ernzerhof[28], is used for the exchange-correlation calculation. To locate transition states (TS), the NEB[29] and Dimer methods[30, 31] are used. A four-layer, $p(4 \times 4)$ slab with 16 metal atoms in each layer is used as surface model. The top two layers are relaxed, while the bottom two layers are fixed. A vacuum space of 15 Å is used to minimize the interactions of two successive metal surfaces in Z direction.

Cluster model DFT calculations in vacuum are carried out with the TURBOMOLE 6.5 program package.[32, 33] The cluster models are obtained by removal of the periodic boundary conditions from the periodic slabs that were optimized from our previous plane-wave (VASP) calculations. The cluster model consists of two layers with a total number of 51 Ru atoms (see Figure S1). A convergence test for solvation energy with respect to the metal cluster size can be found elsewhere.[44] All adsorbate atoms are represented by all-electron TZVP[35-37] basis sets, while Ru atoms are represented by ecp-28-mwb-TZVP effective core potentials (ECPs), together with TZVP basis sets for the valence electrons. The Coulomb potential is approximated with the RI-J approximation using auxiliary basis sets.[38-40] The self-consistent field (SCF) calculation is converged to an energy-based convergence criterion of 1.0×10^{-7} Hartree. The lowest spin state is found based on single-point energy calculations for different spin states. Then, COSMO calculations for the cluster models in the aqueous phase are performed on the same lowest energy spin state configurations at the same level of theory. The dielectric constant was set to infinity as required for COSMO-RS[41, 42] calculations. Default radii-based cavities of Ru atoms (2.223 Å) in the TURBOMOLE program package, a 10% increased (2.445 Å), and a 10% decreased (2.0007 Å) value were used for cavity construction since the cavity radius of Ru is likely not optimized given the ambiguity associated with the interpretation of the cavity radius of transition metal atoms in implicit solvation models and the lack of available experimental data.[43]

For solvent effect calculations, we have used the implicit solvation model for solid surfaces (*iSMS*) method.[44] The fundamental idea of this method is a simple subtractive scheme:

$$G^{liquid}_{surface\,+\,intermediate} = G^{vacuum}_{surface\,+\,intermediate} + \left(G^{liquid}_{cluster\,+\,intermediate} - E^{vacuum}_{cluster\,+\,intermediate}\right) \tag{1}$$

where $G^{liquid}_{surface\,+\,intermediate}$ is the Gibbs free energy of an intermediate adsorbed on the surface in a liquid phase environment, $G^{vacuum}_{surface\,+\,intermediate}$ is the free energy in the absence of a solvent, computed within the harmonic approximation using plane-wave DFT calculations for periodic slab models, and $G^{liquid}_{cluster\,+\,intermediate}$ is the free energy (without vibrational contributions) of the surface species when the surface cluster model is immersed in an implicit solvent (which is obtained by extracting selected metal atoms and removing the periodic boundary conditions). We note that $G^{liquid}_{cluster\,+\,intermediate}$ does not contain vibrational contributions of the adsorbate that are already considered in the first term. Finally, $E^{vacuum}_{cluster\,+\,intermediate}$ is the DFT energy of the same cluster in the absence of the solvent.

It has recently been shown that aqueous solvent effects on the adsorption strength of aromatic molecules such as phenol are highly endergonic. In contrast, implicit solvation models tend to predict an exergonic solvent effect.[55] Likely, the origin for this difference is an underprediction of the cavity formation energy in implicit solvation models. Consequently, implicit solvation models are expected to possess significant errors for adsorption processes but are possibly reasonably accurate for surface processes that do not involve large changes in cavity size. It should be noted that hydrogen bonding contributions are implicitly parameterized in the Conductor like Screening Model (COSMO) and that *iSMS* has been shown to perform reasonably well for neutral species[34, 45-47] and for reactions when hydrogen bonding contributions do not change significantly along the reaction coordinate.[48]

The COSMOtherm[49] database for solvent thermodynamic properties with BP-TZVP parametrization and COSMO calculation results for all other structures at the BP-TZVP level of theory are used to determine the free energy of the cluster in water. It is worth noting that the parametrization combination of BP functional and basis sets of triple-ξ quality (TZVP) were used for COSMOtherm calculations since it is recommended for high quality predictions of thermophysical data for chemical engineering purposes by the COSMOtherm user manual.

2.2. Microkinetic Model

To construct the microkinetic models, the reaction rates for all surface reactions were calculated as

$$r = k_f \prod_m \theta_m^{s_m} - k_r \prod_n \theta_n^{s_n} \tag{2}$$

where k_f and k_r denote forward and reverse rate constants, θ_m and θ_n are the normalized surface coverage of reactants, m, and products, n, and s_m and s_n represent the stoichiometric coefficients. We used harmonic transition state theory (hTST) to calculate rate constants

$$k_f = \frac{k_B T}{h} e^{\frac{-\Delta G^{\ddagger}}{k_B T}} \tag{3}$$

where k_B is the Boltzmann constant, T represents the reaction temperature, h is the Planck constant, and $\Delta G^{\ddagger}$ denotes the activation free energy at the corresponding temperature. The vapor-phase free energy of activation is calculated utilizing the zero-point correction and vibrational partition functions as

$$\Delta G^{\ddagger} = \Delta E_{scf}{}^{\ddagger} + \Delta E_{ZPE}{}^{\ddagger} - k_B T \, ln \frac{q_{vib}^{TS}}{q_{vib}^{Reactant}} \tag{4}$$

$$E_{ZPE} = \frac{1}{2} \sum_i h v_i \quad , \quad q_{vib} = \prod_i \frac{1}{1 - e^{\frac{-h v_i}{k_B T}}} \tag{5}$$

where v_i is the harmonic vibrational frequency. In addition, the aqueous-phase activation free energy ($\Delta G_{solvent}^{\ddagger}$) and reaction free energy ($\Delta G_{solvent}^{rxn}$) are calculated as:

$$\Delta G_{solvent}^{\ddagger} = \Delta G_{Gas}^{\ddagger} + \left[G_{solvent}^{TS} - G_{solvent}^{IS} \right] \tag{6}$$

$$\Delta G_{solvent}^{rxn} = \Delta G_{Gas}^{rxn} + \left[G_{solvent}^{FS} - G_{solvent}^{IS} \right] \tag{7}$$

where $G_{solvent}^{IS}$, $G_{solvent}^{TS}$, and $G_{solvent}^{FS}$ represent the solvation free energies of the initial, transition, and final states, respectively, and $\Delta G_{Gas}^{\ddagger}$ and ΔG_{Gas}^{rxn} are the activation and the reaction free energies under vapor-phase conditions, respectively. For adsorption/desorption reactions, collision theory was used with a sticking coefficient of 1.

$$k_{for} = \frac{1}{N_0\sqrt{2\pi m_A k_B T}} \tag{8}$$

where m_A is the molecular weight of adsorbent A, and N_0 denotes the number of sites per unit area ($1.56 \times 10^{19}\ m^{-2}$). The reverse rate constants (k_{rev}) are calculated using

$$k_{rev} = \frac{k_{for}}{K} \tag{9}$$

where the equilibrium constant, K, is computed as

$$K = e^{\frac{-\Delta G^{ads}}{k_B T}} \tag{10}$$

The adsorption free energy in solvent ($\Delta G^{ads}_{solvent}$) is obtained by the following formula

$$\Delta G^{ads}_{solvent} = \Delta G^{ads}_{Gas} + \left[G^{A^*}_{solvent} - G^{*}_{solvent}\right] \tag{11}$$

where ΔG^{ads}_{Gas} is the adsorption free energy in the vapor phase and $G^{A^*}_{solvent}$ and $G^{*}_{solvent}$ are the solvation free energies of adsorbent A and the clean surface immersed in the solvent, respectively. All forward and reverse rate constants are used to solve all nonlinear steady-state equations simultaneously under defined reaction conditions (differential conversion) to obtain the surface coverages and reaction rates.

The partial pressure/fugacity of fluid phase molecules for our microkinetic model were determined based on an experimental measurement from Ferrin et al.[17] such that the ethanol, hydrogen, and CH_4 partial pressures were set to 0.80, 0.2, and 0.002 bar, respectively, in all of our microkinetic modeling calculations in the vapor and aqueous phases. In addition, we set the partial pressure/fugacity of our main products (CO, C_2H_6, CH_3OH, C_2H_4, C_2H_2, CO_2, CH_3CHO, CH_2O) to 1.0×10^{-20} bar in all phases. Small, but non-zero, product partial pressures often improve the convergence properties of the microkinetic models. In the vapor phase model, we also set the water partial pressure to 1×10^{-20} bar which corresponds to dry reaction conditions. Select calculations with higher water vapor partial pressure have also been performed and are described in section 3.2. In the aqueous phase model, we have assumed vapor-liquid equilibrium (VLE) for water since water is not only a solvent, but also one of the products in the equilibrated vapor phase. The water partial pressure is therefore obtained using the water chemical potential as:

$$x_{H_2O} f^L_{H_2O} = y_{H_2O} P_{tot} = P_{H_2O} \tag{12}$$

where x_{H_2O} is the mole fraction of water in the liquid phase, $f^L_{H_2O}$ is the pure water fugacity at reaction conditions, y_{H_2O} is the water mole fraction in the vapor phase, P_{tot} is the total pressure of the system, and P_{H_2O} indicates the water partial pressure. Assuming a dilute solution ($x_{H_2O} = 1$) and the pure water fugacity at desired temperature obtained from a steam table and a Lee/Kesler Generalized-correlation table,[50] the partial pressure of water is computed at different temperatures (P_{H2O} (473 K) = 15.54 bar, and P_{H2O} (523 K) = 39.74 bar) and used in our microkinetic model in the aqueous-phase study.

2.3. Lateral interactions

Initial results of our microkinetic model indicated that surface H, CO, and O are the most abundant species on the surface. Hence, to approximate a realistic reaction environment, we have included lateral interaction functional forms in our microkinetic model. We used a two-parameter lateral interaction model proposed by Grabow et al.[51] due to its simplicity and ability to obtain reasonable surface coverages. Table S1 of the supporting information includes the functional forms of the lateral interactions used in our microkinetic models. The surface coverages of the most abundant species after applying lateral interaction corrections are summarized in Table 3.

3. Result and Discussion

3.1. Aqueous-phase effects on elementary reactions and strength of adsorption

We studied aqueous-phase effects on ethanol decomposition using a comprehensive reactions network consisting of 133 elementary reactions displayed in Figure 1. The aqueous-phase effect on the adsorption strength of intermediates as well as on reaction and activation free energies of the elementary reactions at 473 and 523 K are shown in Table 1 and 2. Ethanol can start to decompose through five different bond cleavages, via O-H bond cleavage (step 2), dehydrogenation of the α-carbon (step 3), dehydrogenation of the β-carbon (step 4), direct dehydroxylation (step 69), or direct C-C bond cleavage (step 84). All three dehydrogenation reactions (steps 2, 3, and 4) are competitive in the vapor phase with similar (moderate) activation barriers ($\Delta G_2^{Gas,473K} = 0.52, \Delta G_3^{Gas,473K} = 0.58\ eV, \Delta G_4^{Gas,473K} = 0.60\ eV$). These remain competitive in an aqueous phase environment ($\Delta G_2^{liq,473K} = 0.50\ eV, \Delta G_3^{liq,473K} = 0.58\ eV,$ $\Delta G_4^{liq,473K} = 0.59\ eV$). In contrast, direct dehydroxylation in step 69 and direct C-C bond-breaking in step 84 are kinetically demanding in both vapor and aqueous phases ($\Delta G_{69}^{Gas,473K} = 1.56\ eV, \Delta G_{69}^{Gas,473K} = 1.55\ eV, \Delta G_{84}^{Gas,473K} = 2.40\ eV, \Delta G_{84}^{Gas,473K} = 2.37\ eV$).

The reaction network in Figure 1 illustrates that two light hydrocarbons (C_2H_4 and C_2H_6) can be formed by direct dehydroxylation of ethanol in step 69 to form a CH_3CH_2 intermediate, followed by either dehydrogenation of the β-carbon for ethylene production (step 49) or hydrogenation of the α-carbon for ethane production (step 119). Although the desorption of these light hydrocarbons is facilitated in water ($\Delta\Delta G_{C_2H_4}^{desorption,473K} = -0.08\ eV, \Delta\Delta G_{C_2H_6}^{desorption,473K} = -0.08\ eV$), their production remains negligible in an aqueous environment due to the large activation barriers for direct dehydroxylation of ethanol. A similar conclusion can be reached for methanol formation given the larger than 2 eV free energy barriers for C-C bond cleavage of ethanol in step 84 in all reaction environments.

Next, the kinetically most influenced reactions by an aqueous phase environment are reaction steps 32 ($CHCH_2O^* + {}^* \leftrightarrow CHCHO^* + H^*$) and 67 ($CHO^* + {}^* \leftrightarrow CO^* + H^*$). The solvent stabilizes these transition states by 0.27 and 0.12 eV, respectively. Generally, it can be observed from Table 2 that the solvent effect on the free energies of reactions (ranging from -0.10 to +0.10 eV), and the free energies of activation (ranging from -0.10 to 0.05 eV) are predicted to be small.

3.2. Activity and Selectivity

The reaction network can be divided into two major pathways: those involving C-C bond cleavages and those involving C_2 products. As discussed in the introduction, an excellent catalyst for hydrogen production from ethanol reforming should facilitate C-C bond cleavages relative to C-O bond cleavages, facilitate the WGS, and inhibit the methanation reaction that consumes large amounts of hydrogen. Table S2 of the supporting information displays the predicted TOFs of all elementary reactions involved in the ethanol decomposition over the Ru(0001) catalyst surface model at two different temperatures, 473K and 523K, in vapor and aqueous reaction conditions. The overall TOF is also included in Table 4 at different temperatures in the vapor and aqueous phases with default cavity radius for all elements including the Ru atoms from the TURBOMOLE program package and with a 10% increased and decreased cavity radius for the Ru atoms (all other cavity radii are well optimized and we employ TURBOMOLE default values).

In the vapor phase, the TOF for the C-C cleavage product (CO) was found to be 0.12 s^{-1} at 523 K which is in good agreement with the experimental observation of Ferrin et al. (TOF_{CO} = 0.04 s^{-1}).[17] However, Ferrin et al. also reported a C-O cleavage product (C_2H_6) turnover frequency of 3.50×10^{-4} s^{-1}, which is 4 orders of magnitude higher than our computational prediction ($TOF_{C_2H_6} = 9.49\times10^{-8}$ s^{-1}). Sturm et al. also studied ethanol decomposition over terrace sites of Ru by TPD and RAIRS and did not observe any C-O cleavage products.[56] Thus, we conclude that the ethane produced in the study by Ferrin et al. originates likely from more open Ru sites such as Ru step sites. Next, important selectivities in the vapor and aqueous phases are shown in Table 5 and plotted in Figure 3. In the vapor phase and at 473 K, the C-C bond cleavage selectivity (sum of all C1 species selectivities) is about 71%. Half of this selectivity originates from CH formation and the other half from CO formation. Given the selectivity of CO and CH_4 of $S_{CO} = 29\%\ and\ S_{CH_4} = 39\%$, it becomes apparent that while all formed surface CH species become methane via hydrogenation, about 10% of the adsorbed CO undergoes methanation while the rest desorbs as CO (we hardly observe any WGS under dry vapor phase conditions). In contrast, in an aqueous reaction environment at 473 K, the C-C cleavage selectivity is about 50%, methanation barely occurs (about 1%) and nearly all adsorbed CO becomes CO_2 through the WGS reaction ($S_{CO} = 0.0\%, S_{CO_2} = 24\%$). We note that again all surface CH species get hydrogenated to methane ($S_{CH_4} = 26\%$). In addition, the C_2 product is mainly acetaldehyde (CH_3CHO) in both phases which is produced via dehydrogenation of the ethoxy intermediate (CH_3CH_2O) in reaction 5 (see Figure 2). Although the C_2 product selectivity is comparable at the reaction conditions, our calculations suggest a low equilibrium constant for acetaldehyde formation ($C_2H_5OH(g) \leftrightarrow C_2H_4O(g) + H_2(g)$, $K_{eq}^{473K} = 0.08, K_{eq}^{523K} = 0.43$), indicating that at significant ethanol conversion, acetaldehyde formation reaches equilibrium and the C_2 product pathway is suppressed. We also note that increasing the temperature does not significantly affect the product selectivity in the vapor and aqueous phases.

Next, Figure 3 shows the H_2 selectivity on the secondary y-axis. We define it here as the number of H_2 molecules produced per ethanol molecule consumed ($S_{H_2} = {}^{TOF_{H_2}}\!/_{TOF_{CH_3CH_2OH}}$). At 473 K and in the (dry) vapor phase, only 0.84 H_2 molecules are produced per consumed ethanol molecule. In contrast, in the aqueous phase, 1.45 H_2 molecules are formed per ethanol molecule consumed as a result of an accelerated WGS and suppression of the methanation reaction. To understand the dramatic difference in WGS/methanation between (dry) vapor and aqueous phases, we recalculated the vapor phase TOF of H_2 production at a higher water chemical potential (P_{H_2O} = 1×10^{-10} bar to 15.54 bar). Only at a water chemical potential of 1×10^{-3} bar does the H_2 production rate per consumed ethanol increase to 0.85 and at a water partial pressure of 15.54 bar it can be as high as 1.65. Thus, the results indicate that the accelerated WGS under aqueous phase reforming conditions originates primarily from a higher water chemical potential and not from a solvation effect on the elementary surface processes under the APR conditions, which were found to be minimal (Table 2).

3.3. Dominant pathway in vapor and water

A schematic representation of the dominant pathways in vapor and aqueous phase reaction conditions is displayed in Figure 2. Ethanol decomposition follows in both phases the same dominant mechanism up to the production of CH and CO: two successive dehydrogenations of ethanol to acetaldehyde formation on the surface, which can be either desorbed or, followed by two additional dehydrogenation steps, form a CHCO intermediate, which (by C-C cleavage) is then converted to CH and CO ($CH_3CH_2OH \xrightarrow{2} CH_3CH_2O \xrightarrow{5} CH_3CHO \xrightarrow{18,19} CH_2CHO$ or $CH_3CO \xrightarrow{27,31} CH_2CO \xrightarrow{40} CHCO \xrightarrow{106} CH+CO$). The observation of a C-C bond cleavage through a ketenyl species (CHCO) agrees well with the experimental observation of Ferrin et al.[17] Once these two species (CH & CO) are formed on the surface, the dominant mechanism bifurcates in the two reaction environments. In the vapor phase, methane formation is favorable through successive hydrogenations of the CH intermediate in reaction steps 60, 59, and 123, and CO mainly desorbs from the surface (step 122). But, about 5-10% of the CO (dependent on temperature; see Table 5 and Figure 3) undergoes a methanation reaction. CO_2

production is relatively small under these (dry) reaction conditions, as surface O and OH species have to be produced from CHOH, COH, and CCHOH species that prefer dehydrogenation steps over C-OH cleavage steps. In contrast, in the aqueous phase, nearly all CO produced is converted to CO_2 (step 130) through the WGS reaction that competes with methane formation (almost equal CH_4 and CO_2 selectivity; see Table 5 and Figure 3). Under APR conditions, the WGS can occur on a Ru surface by direct water dissociation to produce surface oxygen species that combined with surface CO to CO_2.[57] The hydrogen production rate in the aqueous phase (high water chemical potential) is higher than the ethanol consumption rate (see step 1 and 124 in Table S2), clearly indicating that the WGS occurs under these reaction conditions. Thus, we conclude that in the presence of liquid water and a corresponding high water fugacity, the hydrogen selectivity is significantly increased, although the overall ethanol decomposition and hydrogen production rate is decreased over Ru(0001).

4. Sensitivity analysis, apparent activation barriers, and reaction orders

First, Campbell's degree of rate control,[52-54] $X_{RC,i}$, was used to investigate the sensitivity of each transition state on the overall rate of ethanol decomposition over a Ru(0001) catalyst surface model.

$$X_{RC,i} = \frac{k_i}{r}\left(\frac{\partial r}{\partial k_i}\right)_{K_i,\ k_j \neq k_i} \tag{15}$$

where r is the overall reaction rate, k_i is the forward rate constant for step i, and K_i is the equilibrium constant for step i. The sensitivity analysis reveals that reaction step 2 ($CH_3CH_2OH^*$ + * $\leftrightarrow$ $CH_3CH_2O^*$ + H^*) possesses the most sensitive transition state in both vapor and aqueous phases ($X_{rc,2}^{Gas} = 0.68,\ X_{rc,2}^{Liq} = 0.71$). Reaction steps 3 and 4, two other dehydrogenation steps of ethanol, are other important reactions in our sensitivity analysis ($X_{rc,3}^{Gas} = 0.20,\ X_{rc,3}^{Liq} = 0.17;\ X_{rc,4}^{Gas} = 0.15,\ X_{rc,4}^{Liq} = 0.13$). This observation of initial dehydrogenation reactions being key to the reaction network agrees with earlier studies of Vlachos et al. and López et al.[58,59]

Next, the apparent activation barriers were computed in the temperature ranges of 473 to 573 K in both reaction environments.

$$E_a = RT^2\left(\frac{\partial \ln(r)}{\partial T}\right)_{p_i} \tag{16}$$

The Arrhenius plot in Figure 4 displays that since the rate controlling steps are similar in all reaction environments, the apparent activation barriers are very similar for ethanol decomposition in the vapor and aqueous phases ($E_a^{Gas} = 1.06\ eV$, $E_a^{Liq} = 1.11\ eV$).

Finally, the reaction orders with respect to the partial pressure of ethanol, carbon monoxide, methane and hydrogen were calculated at 523 K and a pressure range of 0.1 to 10 bar for CH_3CH_2OH, 1×10^{-10} to 1×10^{-5} bar for CO (at a CO partial pressure > 1×10^{-5} bar, the surface gets poisoned by CO), 0.002 to 0.1 bar for CH_4, and 0.4 to 40 bar for H_2.

$$a_i = \left(\frac{\partial \ln(r)}{\partial \ln(p_i)}\right)_{T, p_{j \neq i}} \tag{17}$$

The overall reaction rate is first-order and zero-order with respect to ethanol and carbon monoxide, respectively, irrespective of reaction environment. On the other hand, the reaction order of methane is -0.28 and -0.19 in the vapor phase and in the aqueous phase, respectively. In both reaction environments, an increase in methane partial pressure results in the catalyst surface getting poisoned by methylidyne species (CH) which explains the negative reaction order of methane. Finally, the reaction rate is inversely proportional to hydrogen partial pressure in the vapor and aqueous phases ($a_{H_2}^{Gas} = -1.07$, $a_{H_2}^{Liq} = -1.03$) demonstrating that ethanol reforming is ideally coupled with a hydrogen consumption process in a tandem reaction typical for aqueous-phase processing of biomass for hydrocarbon fuel and chemical production.

Conclusion

Ethanol decomposition over a Ru(0001) catalyst surface model has been investigated in vapor and aqueous phase environments. A reaction network comprised of 133 elementary reactions has been studied with the help of density functional theory to compute kinetic and thermodynamic parameters of the various elementary vapor phase reactions. Solvent effects on elementary reactions and the adsorption strength of all intermediates have been studied using the implicit solvation model for solid surfaces (*iSMS*). After acquiring the kinetic parameters in the vapor and aqueous phases, a microkinetic reactor model has been developed to obtain the surface coverages and turnover frequencies. Both, the vapor- and the aqueous-phase ethanol decomposition share a similar dominant pathway up to the production of CH and CO as following: two successive dehydrogenations of ethanol to acetaldehyde formation, followed by two further dehydrogenation steps to form a surface CHCO intermediate, which by C-C bond cleavage is then converted to CH and CO ($CH_3CH_2OH \xrightarrow{2} CH_3CH_2O \xrightarrow{5} CH_3CHO \xrightarrow{18, 19} CH_2CHO$ or $CH_3CO \xrightarrow{27, 31} CH_2CO \xrightarrow{40} CHCO \xrightarrow{106} CH+CO$). In the vapor phase the reaction pathway proceeds by complete hydrogenation of CH to form CH_4 and adsorbed CO that desorbs from the surface (90%) or undergoes methanation (10%). In contrast, in the aqueous phase, the methanation is suppressed and CO is converted by the WGS to CO_2 and H_2. Although the overall turnover frequency and C-C bond cleavage selectivity is smaller in the presence of water relative to the vapor phase, the aqueous-phase reaction environment leads to a higher H_2 production efficiency. The higher H_2 production rate in conjunction with a methanation suppression in the aqueous phase results from the presence of a higher water chemical potential in the aqueous phase. Solvation effects computed with implicit solvation models are predicted to be small and hardly affect the H_2 production efficiency.

Associated Content

Supporting Information

Lateral interaction parameters used for the microkinetic models, calculated turnover frequencies of elementary reactions in vapor and aqueous phases at 473 and 523 K, and atomic coordinates of the adsorbed intermediates and transition states involved in the reaction network.

Declaration of Competing Interest

The authors declare that they have no known competing financial interests or personal relationships that could have appeared to influence the work reported in this paper.

Acknowledgements

We gratefully acknowledge financial support from the U.S. Department of Energy, Office of Basic Energy Science, Catalysis Science program under Award DE-SC0007167. In addition, this work was partially supported by the South Carolina Smart State Center for Strategic Approaches to the Generation of Electricity (SAGE). Computational resources have been provided by the National Energy Research Scientific Computing Center (NERSC) under Contract No. DE-AC02-05CH11231 which is supported by the Office of Science of the U.S. Department of Energy. XSEDE resources provided by the San Diego Supercomputer Center (SDSC) and Texas Advanced Computing Center (TACC) under grant number TG-CTS090100 and Environmental Molecular Sciences Laboratory (EMSL) located at Pacific Northwest National Laboratory (Ringgold ID 130367, Grant Proposals 50576 and 51163) were also used for selected DFT calculations. Finally, computing resources from the USC High Performance Computing Group are gratefully acknowledged.

Table 1. Aqueous-phase effect on the stability of various adsorbed species in the ethanol decomposition over a Ru(0001) catalyst surface model at 473 and 523 K. $\Delta\Delta G_{rxn}$indicates the difference in the adsorption free energy of the corresponding intermediate in the presence and the absence of the solvent.

Adsorbate	$\Delta\Delta \boldsymbol{G_{rxn}}, \boldsymbol{eV}$	
	473K	**523K**
CH_3COH	0.10	0.10
CH_3CH_2O	0.10	0.10
CH_3CH_2	0.09	0.09
CH_3OH	0.08	0.09
CH_3CH_2OH	0.08	0.08
CH_3CH_3	0.08	0.08
CHCH	0.08	0.08
CH_2CH_2	0.08	0.08
CH_2CH_2OH	0.08	0.08
CH_2CHOH	0.07	0.08
CH_2CH_2O	0.07	0.07
CHCOH	0.07	0.07
CH_3	0.07	0.07
CH_3CH	0.07	0.07
CH_2COH	0.07	0.07
CH_3CO	0.07	0.07
CH_2OH	0.06	0.07
CH_2CH	0.06	0.06
CH_3CHOH	0.06	0.06
CH_3CHO	0.06	0.06
$CHCH_2OH$	0.06	0.06
CH_3C	0.05	0.05
CCO	0.05	0.05
CHO	0.05	0.05
CH_2	0.04	0.04
$CHCH_2O$	0.04	0.04
CH_2C	0.04	0.04
CH_2CHO	0.04	0.04
CHOH	0.04	0.05
CH_2O	0.04	0.04
CHCHO	0.04	0.04
CHCHOH	0.04	0.04
OH	0.04	0.04
CO	0.03	0.03
CCH	0.03	0.03
CCH_2OH	0.03	0.03
CHCO	0.03	0.03
CH_2CO	0.02	0.03
CH	0.02	0.02
CCOH	0.01	0.02
CCHOH	0.01	0.02
COH	0.01	0.02
H	0.01	0.01
O	0.01	0.01
CCH_2O	0.01	0.01
CCHO	0.01	0.01
CC	0.00	0.00
C	0.00	0.00
CO_2	0.06	0.05

Table 2. Reaction and activation free energies of the elementary reactions for ethanol decomposition over a Ru(0001) catalyst surface model at 473 K and 523 K in vapor phase and under aqueous phase reforming (APR) conditions. Asterisk (*) represents a surface adsorption site and multiple asterisks are indicative of the number of occupied active sites.

Reactions	$\Delta G_{rxn}, eV$				$\Delta G_{act}, eV$			
	473 K		523 K		473 K		523 K	
	Vapor	APR	Vapor	APR	Vapor	APR	Vapor	APR
1. $CH_3CH_2OH + * \leftrightarrow CH_3CH_2OH*$	0.45	0.53	0.62	0.70	N/A	N/A	N/A	N/A
2. $CH_3CH_2OH* + * \leftrightarrow CH_3CH_2O* + H*$	-0.73	-0.70	-0.71	-0.69	0.52	0.50	0.52	0.51
3. $CH_3CH_2OH* + * \leftrightarrow CH_3CHOH* + H*$	-0.09	-0.11	-0.08	-0.09	0.58	0.58	0.60	0.60
4. $CH_3CH_2OH* + * \leftrightarrow CH_2CH_2OH* + H*$	-0.17	-0.17	-0.15	-0.14	0.60	0.59	0.62	0.62
5. $CH_3CH_2O* + * \leftrightarrow CH_3CHO* + H*$	-0.01	-0.04	0.00	-0.03	0.62	0.59	0.62	0.60
6. $CH_3CH_2O* + * \leftrightarrow CH_2CH_2O* + H*$	0.12	0.10	0.13	0.12	0.78	0.77	0.79	0.78
7. $CH_3CHOH* + * \leftrightarrow CH_3COH* + H*$	-0.56	-0.51	-0.57	-0.53	0.18	0.19	0.18	0.18
8. $CH_3CHOH* + * \leftrightarrow CH_2CHOH* + H*$	-0.48	-0.46	-0.48	-0.46	0.36	0.39	0.37	0.39
9. $CH_3CHOH* + * \leftrightarrow CH_3CHO* + H*$	-0.64	-0.63	-0.63	-0.63	0.46	0.45	0.46	0.45
10. $CH_2CH_2OH* + * \leftrightarrow CHCH_2OH* + H*$	-0.46	-0.47	-0.46	-0.47	0.23	0.22	0.24	0.22
11. $CH_2CH_2OH* + * \leftrightarrow CH_2CHOH* + H*$	-0.40	-0.40	-0.41	-0.40	0.29	0.26	0.31	0.28
12. $CH_2CH_2OH* + * \leftrightarrow CH_2CH_2O* + H*$	-0.44	-0.43	-0.43	-0.43	0.48	0.45	0.49	0.46
13. $CH_2CH_2O* + * \leftrightarrow CH_2CHO* + H*$	-0.78	-0.81	-0.79	-0.81	0.27	0.26	0.26	0.26
14. $CH_2CH_2O* + * \leftrightarrow CHCH_2O* + H*$	-0.21	-0.23	-0.21	-0.23	0.32	0.28	0.32	0.29
15. $CH_2CHOH* + * \leftrightarrow CH_2CHO* + H*$	-0.82	-0.84	-0.81	-0.84	0.27	0.26	0.28	0.26
16. $CH_2CHOH* + * \leftrightarrow CH_2COH* + H*$	-0.63	-0.62	-0.62	-0.62	0.00	0.00	0.01	0.00
17. $CH_2CHOH* + * \leftrightarrow CHCHOH* + H*$	-0.60	-0.62	-0.58	-0.60	0.13	0.09	0.14	0.10
18. $CH_3CHO* + * \leftrightarrow CH_2CHO* + H*$	-0.66	-0.67	-0.66	-0.67	0.00	0.00	0.00	0.00
19. $CH_3CHO* + * \leftrightarrow CH_3CO* + H*$	-0.85	-0.83	-0.86	-0.85	0.00	0.00	0.00	0.00
20. $CH_3COH* + * \leftrightarrow CH_2COH* + H*$	-0.55	-0.57	-0.54	-0.55	0.54	0.53	0.55	0.55
21. $CH_3COH* + * \leftrightarrow CH_3CO* + H*$	-0.93	-0.96	-0.93	-0.95	0.33	0.28	0.32	0.28
22. $CHCH_2OH* + * \leftrightarrow CCH_2OH* + H*$	-0.67	-0.69	-0.68	-0.69	0.00	0.00	0.00	0.00
23. $CHCH_2OH* + * \leftrightarrow CHCHOH* + H*$	-0.54	-0.55	-0.53	-0.53	0.20	0.17	0.22	0.20
24. $CHCH_2OH* + * \leftrightarrow CHCH_2O* + H*$	-0.18	-0.19	-0.17	-0.18	0.51	0.47	0.52	0.49
25. $CCH_2OH* + * \leftrightarrow CCH_2O* + H*$	-0.12	-0.13	-0.10	-0.11	0.64	0.65	0.66	0.67
26. $CCH_2OH* + * \leftrightarrow CCHOH* + H*$	-0.34	-0.34	-0.32	-0.32	0.05	0.08	0.06	0.09
27. $CH_2CHO + * \leftrightarrow CH_2CO* + H*$	-0.43	-0.43	-0.43	-0.43	0.07	0.06	0.07	0.06
28. $CH_2CHO + * \leftrightarrow CHCHO* + H*$	-0.40	-0.39	-0.39	-0.38	1.27	1.27	1.27	1.27
29. $CH_2COH + * \leftrightarrow CH_2CO* + H*$	-0.62	-0.65	-0.61	-0.64	0.49	0.47	0.50	0.48
30. $CH_2COH + * \leftrightarrow CHCOH* + H*$	-0.65	-0.64	-0.65	-0.63	0.37	0.38	0.38	0.39
31. $CH_3CO + * \leftrightarrow CH_2CO* + H*$	-0.24	-0.27	-0.22	-0.25	0.38	0.34	0.40	0.36
32. $CHCH_2O + * \leftrightarrow CHCHO* + H*$	-0.97	-0.96	-0.98	-0.97	0.14	0.02	0.23	0.02
33. $CHCH_2O + * \leftrightarrow CCH_2O* + H*$	-0.61	-0.63	-0.60	-0.62	0.32	0.32	0.32	0.32
34. $CHCHOH* + * \leftrightarrow CCHOH* + H*$	-0.47	-0.48	-0.47	-0.49	0.13	0.13	0.13	0.13
35. $CHCHOH* + * \leftrightarrow CHCHO* + H*$	-0.61	-0.60	-0.62	-0.62	0.46	0.45	0.46	0.44
36. $CHCHOH* + * \leftrightarrow CHCOH* + H*$	-0.68	-0.64	-0.69	-0.65	0.29	0.30	0.29	0.29
37. $CCH_2O* + * \leftrightarrow CCHO* + H*$	-0.61	-0.60	-0.61	-0.60	0.06	0.07	0.07	0.08
38. $CCHOH + * \leftrightarrow CCHO* + H*$	-0.39	-0.39	-0.39	-0.39	0.63	0.64	0.64	0.64
39. $CCHOH + * \leftrightarrow CCOH* + H*$	-0.30	-0.29	-0.31	-0.30	0.72	0.72	0.72	0.72
40. $CH_2CO* + * \leftrightarrow CHCO* + H*$	-0.52	-0.51	-0.52	-0.51	0.39	0.40	0.39	0.40
41. $CHCHO* + * \leftrightarrow CCHO* + H*$	-0.25	-0.27	-0.24	-0.26	0.32	0.31	0.33	0.32
42. $CHCHO* + * \leftrightarrow CHCO* + H*$	-0.55	-0.55	-0.56	-0.55	0.60	0.58	0.60	0.58
43. $CHCOH* + * \leftrightarrow CCOH* + H*$	-0.09	-0.14	-0.09	-0.13	0.98	0.95	0.98	0.97
44. $CHCOH* + * \leftrightarrow CHCO* + H*$	-0.49	-0.52	-0.49	-0.52	0.85	0.81	0.85	0.81
45. $CHCO* + * \leftrightarrow CCO* + H*$	-0.34	-0.31	-0.35	-0.32	0.99	0.97	0.98	0.96
46. $CCOH* + * \leftrightarrow CCO* + H*$	-0.74	-0.69	-0.74	-0.71	0.85	0.85	0.86	0.85
47. $CCHO* + * \leftrightarrow CCO* + H*$	-0.65	-0.59	-0.66	-0.62	0.77	0.79	0.76	0.77
48. $CH_3CH_2* + * \leftrightarrow CH3CH* + H*$	-0.74	-0.75	-0.74	-0.75	0.08	0.09	0.09	0.10
49. $CH_3CH_2* + * \leftrightarrow CH_2CH_2* + H*$	-0.60	-0.61	-0.59	-0.59	0.05	0.05	0.06	0.07
50. $CH_3CH* + * \leftrightarrow CH_3C* + H*$	-0.80	-0.81	-0.81	-0.81	0.00	0.01	0.00	0.01
51. $CH_3CH* + * \leftrightarrow CH_2CH* + H$	-0.31	-0.31	-0.30	-0.29	0.27	0.27	0.29	0.29

52. $CH_2CH_2^* + * \leftrightarrow CH_2CH^* + H^*$	-0.45	-0.46	-0.45	-0.45	0.15	0.15	0.15	0.16
53. $CH_2CH^* + * \leftrightarrow CH_2C^* + H^*$	-0.58	-0.59	-0.58	-0.59	0.02	0.02	0.03	0.02
54. $CH_2CH^* + * \leftrightarrow CHCH^* + H^*$	-0.63	-0.61	-0.63	-0.60	0.33	0.34	0.34	0.34
55. $CH_3C^* + * \leftrightarrow CH_2C^* + H^*$	-0.09	-0.09	-0.07	-0.07	0.45	0.46	0.48	0.48
56. $CH_2C^* + * \leftrightarrow CCH^* + H^*$	-0.22	-0.23	-0.22	-0.22	0.62	0.61	0.62	0.62
57. $CHCH^* + * \leftrightarrow CCH^* + H^*$	-0.17	-0.21	-0.17	-0.21	0.54	0.50	0.54	0.50
58. $CCH^* + * \leftrightarrow CC^* + H^*$	0.36	0.34	0.36	0.34	1.12	1.12	1.12	1.11
59. $CH_3^* + * \leftrightarrow CH_2^* + H^*$	-0.36	-0.37	-0.35	-0.36	0.39	0.38	0.40	0.39
60. $CH_2^* + * \leftrightarrow CH^* + H^*$	-0.63	-0.64	-0.63	-0.64	0.01	0.00	0.02	0.01
61. $CH^* + * \leftrightarrow C^* + H^*$	-0.04	-0.05	-0.04	-0.05	0.73	0.72	0.74	0.72
62. $CH_2OH^* + * \leftrightarrow CH_2O^* + H^*$	-0.64	-0.66	-0.63	-0.65	0.51	0.47	0.52	0.48
63. $CH_2OH^* + * \leftrightarrow CHOH^* + H^*$	-0.45	-0.46	-0.44	-0.45	0.17	0.16	0.19	0.18
64. $CH_2O^* + * \leftrightarrow CHO^* + H^*$	-0.54	-0.52	-0.54	-0.52	0.08	0.07	0.08	0.07
65. $CHOH^* + * \leftrightarrow CHO^* + H^*$	-0.73	-0.71	-0.74	-0.73	0.46	0.44	0.46	0.43
66. $CHOH^* + * \leftrightarrow COH^* + H^*$	-1.17	-1.19	-1.18	-1.20	0.00	0.01	0.00	0.00
67. $CHO^* + * \leftrightarrow CO^* + H^*$	-1.23	-1.23	-1.23	-1.24	0.27	0.00	0.34	0.00
68. $COH^* + * \leftrightarrow CO^* + H^*$	-0.78	-0.75	-0.78	-0.77	0.84	0.83	0.85	0.83
69. $CH_3CH_2OH^* + * \leftrightarrow CH_3CH_2^* + OH^*$	-0.46	-0.42	-0.46	-0.41	1.56	1.55	1.56	1.55
70. $CH_3CHOH^* + * \leftrightarrow CH_3CH^* + OH^*$	-1.11	-1.06	-1.12	-1.07	0.31	0.31	0.31	0.30
71. $CH_2CH_2OH^* + * \leftrightarrow CH_2CH_2^* + OH^*$	-0.89	-0.85	-0.89	-0.85	0.74	0.76	0.74	0.74
72. $CH_3COH^* + * \leftrightarrow CH_3C^* + OH^*$	-1.35	-1.36	-1.36	-1.36	0.83	0.80	0.83	0.82
73. $CH_2CHOH^* + * \leftrightarrow CH_2CH^* + OH^*$	-0.94	-0.91	-0.94	-0.91	0.77	0.77	0.78	0.78
74. $CHCH_2OH^* + * \leftrightarrow CHCH_2^* + OH^*$	-0.88	-0.84	-0.88	-0.83	0.78	0.78	0.78	0.78
75. $CH_2COH^* + * \leftrightarrow CH_2C^* + OH^*$	-0.89	-0.88	-0.89	-0.87	0.66	0.65	0.66	0.66
76. $CCH_2OH^* + * \leftrightarrow CCH_2^* + OH^*$	-0.79	-0.74	-0.78	-0.73	0.71	0.73	0.72	0.74
77. $CHCHOH^* + * \leftrightarrow CHCH^* + OH^*$	-0.98	-0.90	-0.99	-0.91	0.63	0.65	0.62	0.63
78. $CCHOH^* + * \leftrightarrow CCH^* + OH^*$	-0.67	-0.62	-0.68	-0.63	0.56	0.58	0.57	0.58
79. $CHCOH^* + * \leftrightarrow CHC^* + OH^*$	-0.46	-0.47	-0.46	-0.46	1.30	1.25	1.31	1.26
80. $CCOH^* + * \leftrightarrow CC^* + OH^*$	-0.02	0.01	-0.02	0.02	1.55	1.53	1.55	1.54
81. $CH_2OH^* + * \leftrightarrow CH_2^* + OH^*$	-1.12	-1.10	-1.11	-1.09	0.55	0.54	0.54	0.54
82. $CHOH^* + * \leftrightarrow CH^* + OH$	-1.30	-1.28	-1.31	-1.28	0.27	0.25	0.26	0.24
83. $COH^* + * \leftrightarrow C^* + OH^*$	-0.17	-0.14	-0.16	-0.13	1.18	1.16	1.20	1.18
84. $CH_3CH_2OH^* + * \leftrightarrow CH_3^* + CH_2OH^*$	0.07	0.12	0.08	0.13	2.40	2.37	2.42	2.39
85. $CH_3CH_2O^* + * \leftrightarrow CH_3^* + CH_2O^*$	0.16	0.17	0.16	0.17	2.14	2.11	2.13	2.10
86. $CH_3CHOH^* + * \leftrightarrow CH_3^* + CHOH^*$	-0.28	-0.23	-0.28	-0.23	1.09	1.08	1.09	1.09
87. $CH_2CH_2OH^* + * \leftrightarrow CH_2^* + CH_2OH^*$	-0.11	-0.08	-0.12	-0.09	1.16	1.14	1.17	1.15
88. $CH_3CHO^* + * \leftrightarrow CH_3^* + CHO^*$	-0.37	-0.31	-0.38	-0.33	0.93	0.96	0.93	0.95
89. $CH_2CH_2O^* + * \leftrightarrow CH_2^* + CH_2O^*$	-0.32	-0.31	-0.32	-0.31	0.78	0.78	0.79	0.78
90. $CH_3COH^* + * \leftrightarrow CH_3^* + COH^*$	-0.90	-0.91	-0.90	-0.90	1.03	1.01	1.04	1.02
91. $CH_2CHOH^* + * \leftrightarrow CH_2^* + CHOH^*$	-0.15	-0.14	-0.15	-0.14	0.80	0.72	0.81	0.75
92. $CHCH_2OH^* + * \leftrightarrow CH^* + CH_2OH^*$	-0.28	-0.25	-0.29	-0.25	0.93	0.91	0.94	0.93
93. $CH_2CHO^* + * \leftrightarrow CH_2^* + CHO^*$	-0.07	-0.02	-0.08	-0.02	0.46	0.48	0.48	0.50
94. $CHCH_2O^* + * \leftrightarrow CH^* + CH_2O^*$	-0.74	-0.72	-0.74	-0.72	0.66	0.67	0.67	0.68
95. $CH_2COH^* + * \leftrightarrow CH_2^* + COH^*$	-0.70	-0.72	-0.71	-0.71	1.28	1.27	1.27	1.27
96. $CHCHOH^* + * \leftrightarrow CH^* + CHOH^*$	-0.19	-0.16	-0.19	-0.17	0.80	0.77	0.80	0.78
97. $CH_3CO^* + * \leftrightarrow CH_3^* + CO^*$	-0.75	-0.71	-0.75	-0.72	0.86	0.82	0.87	0.83
98. $CCH_2OH^* + * \leftrightarrow C^* + CH_2OH^*$	0.35	0.39	0.36	0.39	1.17	1.18	1.18	1.18
99. $CCH_2O^* + * \leftrightarrow C^* + CH_2O^*$	-0.17	-0.14	-0.18	-0.15	0.98	1.02	0.98	1.01
100. $CCHOH^* + * \leftrightarrow C^* + CHOH^*$	0.24	0.27	0.24	0.27	0.92	0.95	0.93	0.94
101. $CH_2CO^* + * \leftrightarrow CH_2^* + CO^*$	-0.87	-0.82	-0.88	-0.84	0.67	0.66	0.67	0.66
102. $CHCHO^* + * \leftrightarrow CH^* + CHO^*$	-0.31	-0.27	-0.31	-0.28	0.37	0.37	0.39	0.39
103. $CHCOH^* + * \leftrightarrow CH^* + COH^*$	-0.68	-0.72	-0.69	-0.72	0.53	0.50	0.54	0.51
104. $CCHO^* + * \leftrightarrow C^* + CHO^*$	-0.10	-0.05	-0.11	-0.07	0.56	0.57	0.57	0.58
105. $CCOH^* + * \leftrightarrow C^* + COH^*$	-0.63	-0.63	-0.64	-0.63	0.68	0.68	0.69	0.69
106. $CHCO^* + * \leftrightarrow CH^* + CO^*$	-0.98	-0.95	-0.98	-0.97	0.40	0.39	0.40	0.39
107. $CCO^* + * \leftrightarrow C^* + CO^*$	-0.67	-0.69	-0.67	-0.69	0.35	0.32	0.37	0.33
108. $CH_3CH_2^* + * \leftrightarrow CH_3^* + CH_2^*$	-0.58	-0.56	-0.58	-0.55	0.89	0.88	0.90	0.89
109. $CH_3CH^* + * \leftrightarrow CH_3^* + CH^*$	-0.47	-0.45	-0.47	-0.44	0.96	0.97	0.97	0.98
110. $CH_2CH_2^* + * \leftrightarrow CH_2^* + CH_2^*$	-0.34	-0.33	-0.34	-0.33	0.91	0.92	0.91	0.92
111. $CH_3C^* + * \leftrightarrow CH_3^* + C^*$	0.29	0.31	0.30	0.32	1.41	1.40	1.42	1.41

112. $CH_2CH^* + * \leftrightarrow CH_2^* + CH^*$	-0.52	-0.51	-0.52	-0.51	1.06	1.05	1.06	1.05
113. $CH_2C^* + * \leftrightarrow CH_2^* + C^*$	0.02	0.03	0.02	0.03	1.68	1.67	1.68	1.67
114. $CHCH^* + * \leftrightarrow CH^* + CH^*$	-0.51	-0.55	-0.51	-0.55	0.74	0.71	0.76	0.72
115. $CCH^* + * \leftrightarrow C^* + CH^*$	-0.39	-0.39	-0.38	-0.39	1.01	1.01	1.02	1.02
116. $CC^* + * \leftrightarrow C^* + C^*$	-0.78	-0.78	-0.78	-0.78	1.11	1.11	1.12	1.12
117. $C^* + O^* \leftrightarrow CO^* + *$	0.26	0.28	0.24	0.25	2.24	2.23	2.24	2.23
118. $OH^* + * \leftrightarrow O^* + H^*$	-0.87	-0.89	-0.86	-0.89	0.67	0.66	0.68	0.65
119. $CH_3CH_2^* + H^* \leftrightarrow CH_3CH_3^* + H^*$	0.13	0.11	0.10	0.08	0.73	0.70	0.72	0.69
120. $CH_2OH^* + H^* \leftrightarrow CH_3OH^* + H^*$	0.17	0.18	0.15	0.16	0.81	0.81	0.81	0.81
121. $H^* + OH^* \leftrightarrow H_2O^* + *$	0.49	0.47	0.46	0.44	1.13	1.09	1.12	1.08
122. $CO^* \leftrightarrow CO(g) + *$	1.21	1.18	1.07	1.04	N/A	N/A	N/A	N/A
123. $CH_3^* + H^* \leftrightarrow CH_4(g) + 2^*$	0.15	0.07	0.00	-0.08	N/A	N/A	N/A	N/A
124. $H^* + H^* \leftrightarrow H_2(g) + 2^*$	0.65	0.63	0.52	0.50	N/A	N/A	N/A	N/A
125.$H_2O^* \leftrightarrow H_2O(g) + *$	-0.27	-0.29	-0.40	-0.44	N/A	N/A	N/A	N/A
126. $CH_3CH_3^* \leftrightarrow CH_3CH_3(g) + *$	-0.70	-0.79	-0.85	-0.92	N/A	N/A	N/A	N/A
127. $CH_3OH^* \leftrightarrow CH_3OH(g) + *$	-0.40	-0.49	-0.56	-0.64	N/A	N/A	N/A	N/A
128. $CH_2CH_2^* \leftrightarrow CH_2CH_2(g) + *$	0.30	0.22	0.13	0.06	N/A	N/A	N/A	N/A
129. $CHCH^{**} \leftrightarrow CHCH(g) + 2^*$	2.31	2.23	2.17	2.09	N/A	N/A	N/A	N/A
130. $CO^* + O^* \leftrightarrow CO_2^* + *$	1.63	1.65	1.61	1.62	N/A	N/A	N/A	N/A
131. $CO_2^* \leftrightarrow CO_2(g) + *$	-0.56	-0.62	-0.67	-0.72	N/A	N/A	N/A	N/A
132. $CH_3CHO^{**} \leftrightarrow CH_3CHO(g) + 2^*$	-0.26	-0.32	-0.36	-0.42	N/A	N/A	N/A	N/A
133. $CH_2O^{**} \leftrightarrow CH_2O(g) + 2^*$	0.20	0.16	0.11	0.07	N/A	N/A	N/A	N/A

Table 3. Surface coverages of most abundant species at 473 K and 523 K in vapor and aqueous phases (APR) obtained from microkinetic modeling of ethanol decomposition over a Ru(0001) catalyst surface model.

	T=473 K		**T=523K**	
	Vapor	**APR**	**Vapor**	**APR**
θ^{*}	0.010	0.012	0.030	0.036
$\theta_{H^{*}}$	0.972	0.974	0.955	0.929
$\theta_{CO^{*}}$	0.011	0.000	0.009	0.000
$\theta_{O^{*}}$	0.000	0.006	0.000	0.011
$\theta_{CH^{*}}$	0.002	0.001	0.005	0.003
$\theta_{OH^{*}}$	0.000	0.006	0.000	0.020
$\theta_{COH^{*}}$	0.006	0.000	0.001	0.000

Table 4. Overall turnover frequencies (ethanol consumption) and H_2 turnover frequencies (hydrogen production) (in s^{-1}) of ethanol decomposition over a Ru(0001) surface in vapor- and aqueous-phase (APR) environments at various temperatures. Aqueous-phase results were obtained using the default cavity radius of Ru atoms in the TURBOMOLE program package, and a 10% incremental change of the default cavity radius of the Ru atoms.

		APR		
T(K)	**Vapor**	**Default**	**-10%**	**+10%**
		Overall TOF		
473	1.31×10^{-2}	3.90×10^{-3}	7.74×10^{-4}	1.97×10^{-3}
498	5.27×10^{-2}	1.59×10^{-2}	8.76×10^{-2}	8.35×10^{-3}
523	1.79×10^{-1}	5.58×10^{-2}	2.12×10^{-1}	3.05×10^{-2}
548	5.06×10^{-1}	1.66×10^{-1}	3.22×10^{-1}	9.44×10^{-2}
573	1.24	4.41×10^{-1}	4.33×10^{-1}	2.59×10^{-1}
		H_2 TOF		
473	1.12×10^{-2}	5.67×10^{-3}	-5.01×10^{-4}	2.66×10^{-3}
498	4.67×10^{-2}	2.32×10^{-2}	6.00×10^{-2}	1.12×10^{-2}
523	1.62×10^{-1}	8.09×10^{-2}	1.79×10^{-1}	4.02×10^{-2}
548	4.64×10^{-1}	2.38×10^{-1}	2.73×10^{-1}	1.22×10^{-1}
573	1.14	6.25×10^{-1}	3.55×10^{-1}	3.31×10^{-1}

Table 5. Selectivities of the different products of the ethanol decomposition over a Ru(0001) catalyst surface model in vapor and aqueous phase (APR) at various temperatures (obtained from turnover frequencies shown in Table S2). For all selectivities, except H_2, the selectivities are defined per carbon atom (and sum to 1.00). For example, the CO selectivity is defined as $TOF_{CO}/(2 * TOF_{CH_3CH_2OH})$ and the acetaldehyde selectivity is $TOF_{CH_3CHO}/TOF_{CH_3CH_2OH}$. Finally, the H_2 selectivity is defined here as $TOF_{H_2}/TOF_{CH_3CH_2OH}$ to show how many H_2 molecules are formed per an ethanol molecule consumed.

	T=473K		**T=498K**		**T=523K**		**T=548K**		**T=573K**	
Selectivity	**vapor**	**APR**	**vapor**	**APR**	**vapor**	**APR**	**vapor**	**APR**	**vapor**	**APR**
CO	0.29	0.00	0.31	0.00	0.32	0.00	0.32	0.00	0.32	0.00
CH_4	0.39	0.25	0.39	0.26	0.38	0.26	0.37	0.26	0.36	0.25
CH_3OH	0.00	0.00	0.00	0.00	0.00	0.00	0.00	0.00	0.00	0.00
CO_2	0.03	0.24	0.02	0.24	0.02	0.24	0.01	0.24	0.01	0.23
CH_3CHO (Acetaldehyde)	0.29	0.51	0.28	0.50	0.28	0.50	0.29	0.51	0.31	0.51
CH_2O (Formaldehyde)	0.00	0.00	0.00	0.00	0.00	0.00	0.00	0.00	0.00	0.00
H_2	0.85	1.45	0.89	1.46	0.91	1.45	0.92	1.43	0.92	1.42

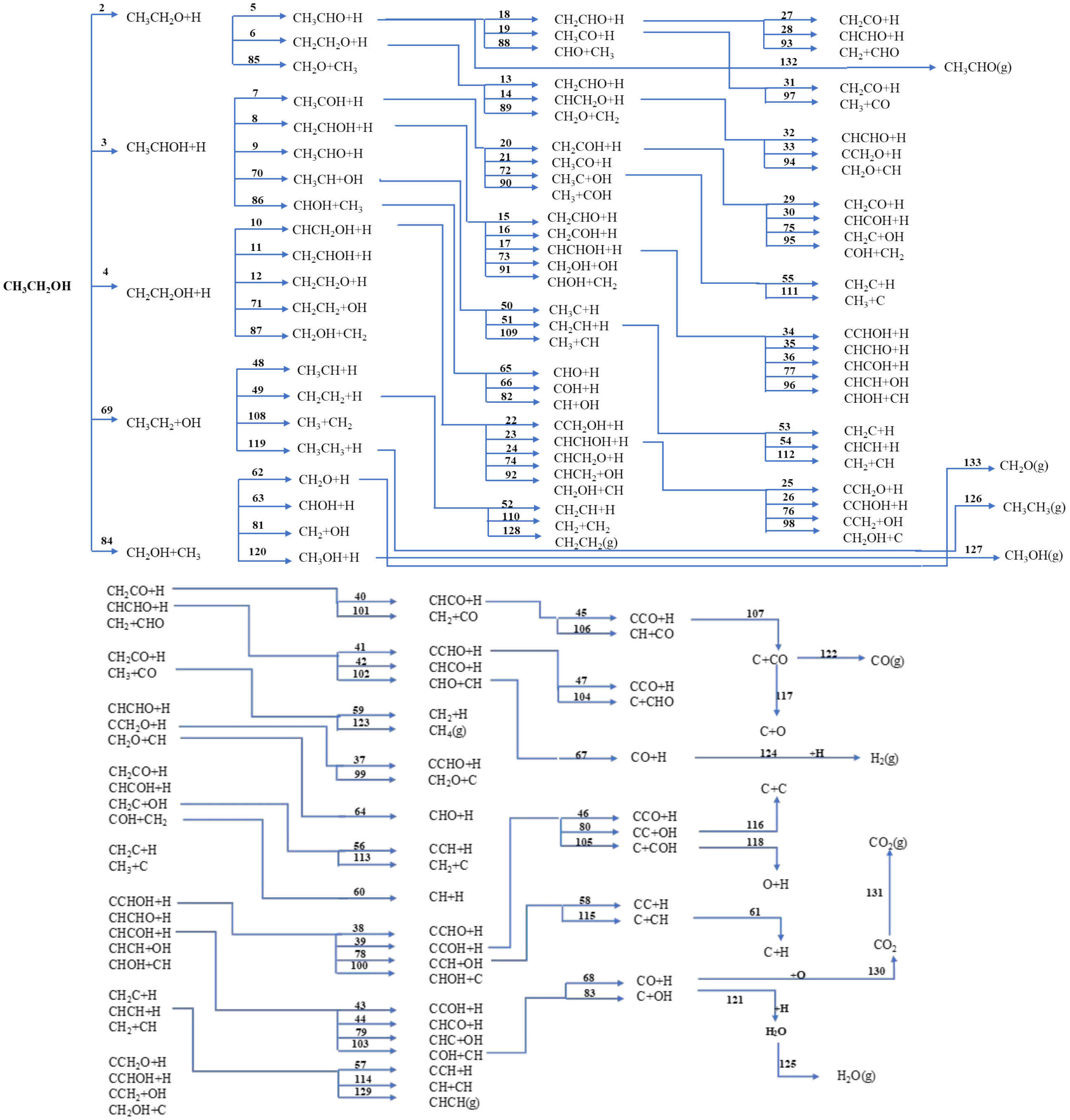

Figure 1. Schematic representation of the reaction network with 133 elementary reactions involved in the ethanol decomposition over a Ru(0001) catalyst surface model.

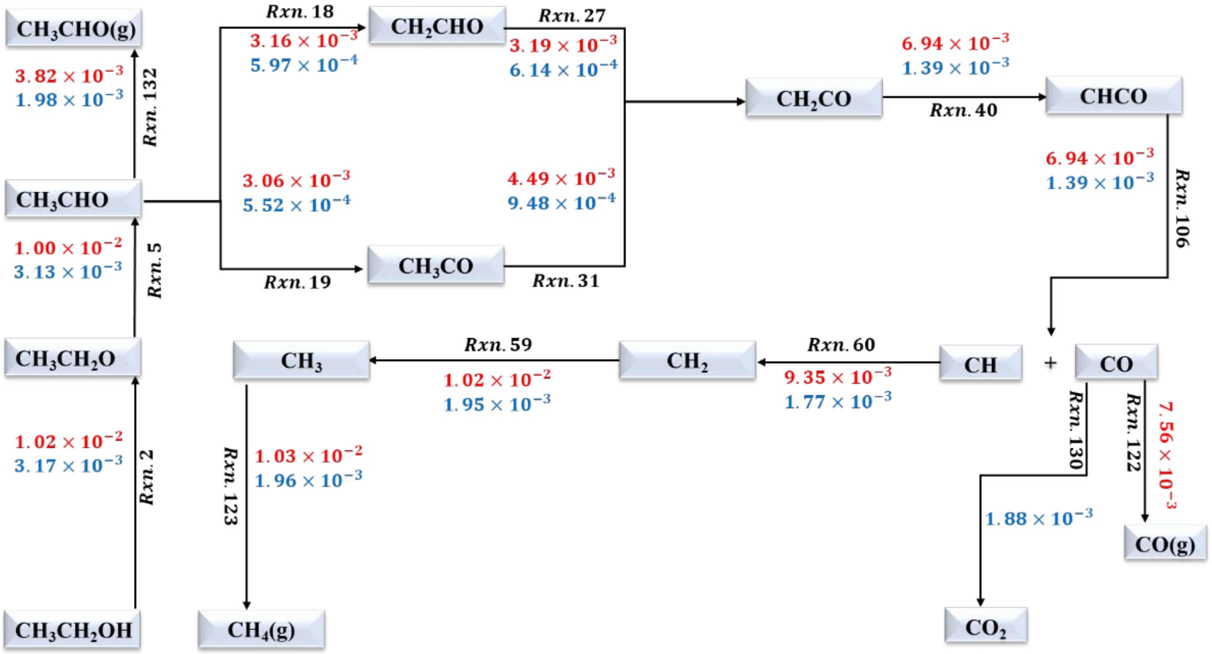

Figure 2. Turnover frequencies (s^{-1}) along the dominant reaction pathway for ethanol decomposition over a Ru(0001) surface in vapor (red color) and aqueous (blue color) phases at 473 K.

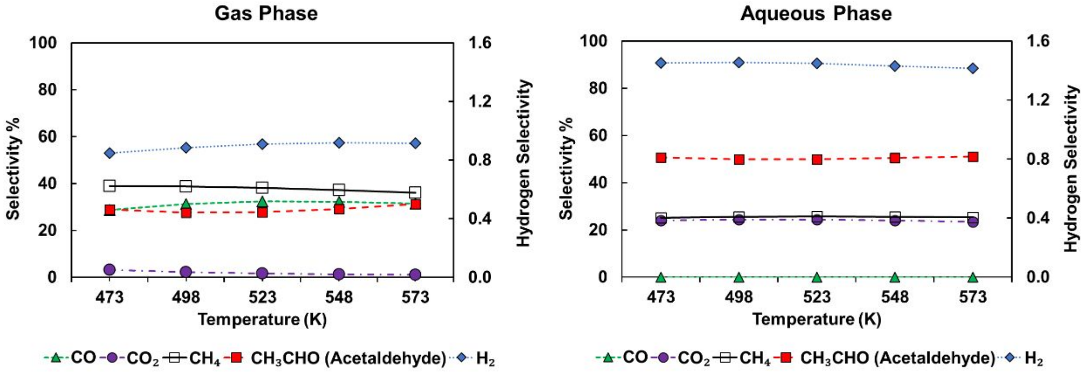

Figure 3. Selectivities of the different products of ethanol decomposition over a Ru(0001) catalyst surface model in (dry) vapor and aqueous phases. We note that for all components except H_2 the defined selectivities are carbon-based (and sum to 1.00). For example, the CO selectivity is defined as $TOF_{CO}/(2 * TOF_{CH_3CH_2OH})$ and the acetaldehyde selectivity is $TOF_{CH_3CHO}/TOF_{CH_3CH_2OH}$. Finally, the H_2 selectivity is defined as $TOF_{H_2}/TOF_{CH_3CH_2OH}$ to show how many H_2 molecules are formed per an ethanol molecule consumed (see Table 5 for selectivity values).

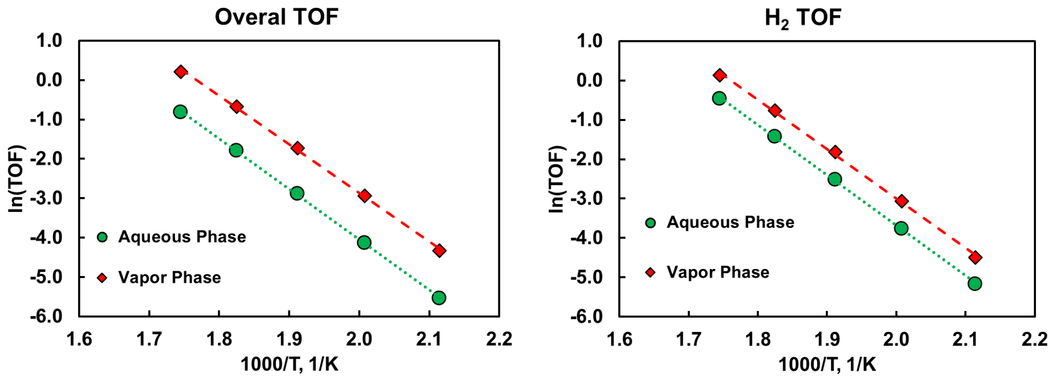

Figure 4. Overall turnover frequencies (ethanol consumption rate) and H_2 production turnover frequencies as a function of inverse temperature in (dry) vapor and aqueous phases over a Ru(0001) catalyst surface model. The apparent activation barrier for ethanol consumption is 1.06 eV in the vapor phase and 1.11 eV in the aqueous phase. The apparent activation barrier of hydrogen production is 1.08 eV in the vapor phase and 1.10 eV in the aqueous phase.

References:

1. Das, D.; Veziroğlu, T. N., Hydrogen production by biological processes: a survey of literature. *International Journal of Hydrogen Energy* **2001,** *26* (1), 13-28.

2. Haryanto, A.; Fernando, S.; Murali, N.; Adhikari, S., Current Status of Hydrogen Production Techniques by Steam Reforming of Ethanol: A Review. *Energy & Fuels* **2005,** *19* (5), 2098-2106.

3. Ni, M.; Leung, D. Y. C.; Leung, M. K. H., A review on reforming bio-ethanol for hydrogen production. *International Journal of Hydrogen Energy* **2007,** *32* (15), 3238-3247.

4. Czernik, S.; Evans, R.; French, R., Hydrogen from biomass-production by steam reforming of biomass pyrolysis oil. *Catalysis Today* **2007,** *129* (3), 265-268.

5. Levin, D. B.; Chahine, R., Challenges for renewable hydrogen production from biomass. *International Journal of Hydrogen Energy* **2010,** *35* (10), 4962-4969.

6. Wang, J. L.; Yin, Y. A., Fermentative hydrogen production using various biomass-based materials as feedstock. *Renew. Sust. Energ. Rev.* **2018,** *92*, 284-306.

7. Arregi, A.; Amutio, M.; Lopez, G.; Bilbao, J.; Olazar, M., Evaluation of thermochemical routes for hydrogen production from biomass: A review. *Energy Conv. Manag.* **2018,** *165*, 696-719.

8. Davda, R. R.; Shabaker, J. W.; Huber, G. W.; Cortright, R. D.; Dumesic, J. A., A review of catalytic issues and process conditions for renewable hydrogen and alkanes by aqueous-phase reforming of oxygenated hydrocarbons over supported metal catalysts. *Applied Catalysis B: Environmental* **2005,** *56* (1), 171-186.

9. Alcalá, R.; Mavrikakis, M.; Dumesic, J. A., DFT studies for cleavage of C⍰C and C⍰O bonds in surface species derived from ethanol on Pt(111). *Journal of Catalysis* **2003,** *218* (1), 178-190.

10. Can, F.; Le Valant, A.; Bion, N.; Epron, F.; Duprez, D., New Active and Selective Rh−REOx−Al2O3 Catalysts for Ethanol Steam Reforming. *The Journal of Physical Chemistry C* **2008,** *112* (36), 14145-14153.

11. Cruz, I. O.; Ribeiro, N. F. P.; Aranda, D. A. G.; Souza, M. M. V. M., Hydrogen production by aqueous-phase reforming of ethanol over nickel catalysts prepared from hydrotalcite precursors. *Catalysis Communications* **2008,** *9* (15), 2606-2611.

12. Tang, Z.; Monroe, J.; Dong, J.; Nenoff, T.; Weinkauf, D., Platinum-Loaded NaY Zeolite for Aqueous-Phase Reforming of Methanol and Ethanol to Hydrogen. *Industrial & Engineering Chemistry Research* **2009,** *48* (5), 2728-2733.

13. Roy, B.; Loganathan, K.; Pham, H. N.; Datye, A. K.; Leclerc, C. A., Surface modification of solution combustion synthesized Ni/Al2O3 catalyst for aqueous-phase reforming of ethanol. *International Journal of Hydrogen Energy* **2010,** *35* (21), 11700-11708.

14. Tokarev, A. V.; Kirilin, A. V.; Murzina, E. V.; Eränen, K.; Kustov, L. M.; Murzin, D. Y.; Mikkola, J. P., The role of bio-ethanol in aqueous phase reforming to sustainable hydrogen. *International Journal of Hydrogen Energy* **2010,** *35* (22), 12642-12649.

15. Godina, L. I.; Heeres, H.; Garcia, S.; Bennett, S.; Poulston, S.; Murzin, D. Y., Hydrogen production from sucrose via aqueous-phase reforming. *International Journal of Hydrogen Energy* **2019,** *44* (29), 14605-14623.

16. Nozawa, T.; Mizukoshi, Y.; Yoshida, A.; Naito, S., Aqueous phase reforming of ethanol and acetic acid over TiO2 supported Ru catalysts. *Applied Catalysis B: Environmental* **2014,** *146*, 221-226.

17. Ferrin, P.; Simonetti, D.; Kandoi, S.; Kunkes, E.; Dumesic, J. A.; Nørskov, J. K.; Mavrikakis, M., Modeling Ethanol Decomposition on Transition Metals: A Combined Application of Scaling and Brønsted−Evans−Polanyi Relations. *Journal of the American Chemical Society* **2009,** *131* (16), 5809-5815.

18. Waheed, A.; Wang, X.; Maeda, N.; Naito, S.; Baiker, A., Surface processes occurring during aqueous phase ethanol reforming on Ru/TiO2 tracked by ATR-IR spectroscopy. *Applied Catalysis A: General* **2019,** *581*, 111-115.

19. Zhao, Z.; Zhang, L.; Tan, Q.; Yang, F.; Faria, J.; Resasco, D., Synergistic bimetallic Ru–Pt catalysts for the low-temperature aqueous phase reforming of ethanol. *AIChE Journal* **2019,** *65* (1), 151-160.

20. Sinfelt, J. H.; Yates, D. J. C., Catalytic hydrogenolysis of ethane over the noble metals of Group VIII. *Journal of Catalysis* **1967,** *8* (1), 82-90.

21. Grenoble, D. C.; Estadt, M. M.; Ollis, D. F., The chemistry and catalysis of the water gas shift reaction: 1. The kinetics over supported metal catalysts. *Journal of Catalysis* **1981,** *67* (1), 90-102.

22. Vannice, M. A., The catalytic synthesis of hydrocarbons from H2CO mixtures over the Group VIII metals: V. The catalytic behavior of silica-supported metals. *Journal of Catalysis* **1977,** *50* (2), 228-236.

23. Kresse, G.; Furthmuller, J., Efficiency of ab-initio total energy calculations for metals and semiconductors using a plane-wave basis set. *Comput. Mater. Sci.* **1996,** *6* (1), 15-50.

24. Kresse, G.; Hafner, J., Ab initio molecular dynamics for liquid metals. *Physical Review B* **1993,** *47* (1), 558-561.

25. Kresse, G.; Joubert, D., From ultrasoft pseudopotentials to the projector augmented-wave method. *Phys. Rev. B* **1999,** *59* (3), 1758-1775.

26. Blöchl, P. E., Projector augmented-wave method. *Phys. Rev. B* **1994,** *50* (24), 17953.

27. Methfessel, M.; Paxton, A. T., High-precision sampling for Brillouin-zone integration in metals. *Physical Review B* **1989,** *40* (6), 3616-3621.

28. Perdew, J. P.; Burke, K.; Ernzerhof, M., Generalized Gradient Approximation Made Simple. *Physical Review Letters* **1996,** *77* (18), 3865-3868.

29. Henkelman, G.; Uberuaga, B. P.; Jónsson, H., A climbing image nudged elastic band method for finding saddle points and minimum energy paths. *The Journal of Chemical Physics* **2000,** *113* (22), 9901-9904.

30. Henkelman, G.; Jónsson, H., A dimer method for finding saddle points on high dimensional potential surfaces using only first derivatives. *The Journal of Chemical Physics* **1999,** *111* (15), 7010-7022.

31. Heyden, A.; Bell, A. T.; Keil, F. J., Efficient methods for finding transition states in chemical reactions: Comparison of improved dimer method and partitioned rational function optimization method. *The Journal of Chemical Physics* **2005,** *123* (22), 224101.

32. Ahlrichs, R.; Bär, M.; Häser, M.; Horn, H.; Kölmel, C., Electronic structure calculations on workstation computers: The program system turbomole. *Chemical Physics Letters* **1989,** *162* (3), 165-169.

33. Treutler, O.; Ahlrichs, R., Efficient molecular numerical integration schemes. *The Journal of Chemical Physics* **1995,** *102* (1), 346-354.

34. Mamun, O.; Saleheen, M.; Bond, J. Q.; Heyden, A., Investigation of solvent effects in the hydrodeoxygenation of levulinic acid to γ-valerolactone over Ru catalysts. *Journal of Catalysis* **2019,** *379*, 164-179.

35. Weigend, F., Accurate Coulomb-fitting basis sets for H to Rn. *Physical Chemistry Chemical Physics* **2006,** *8* (9), 1057-1065.

36. Weigend, F.; Ahlrichs, R., Balanced basis sets of split valence, triple zeta valence and quadruple zeta valence quality for H to Rn: Design and assessment of accuracy. *Physical Chemistry Chemical Physics* **2005,** *7* (18), 3297-3305.

37. Weigend, F.; Häser, M.; Patzelt, H.; Ahlrichs, R., RI-MP2: optimized auxiliary basis sets and demonstration of efficiency. *Chemical Physics Letters* **1998,** *294* (1), 143-152.

38. Eichkorn, K.; Treutler, O.; Öhm, H.; Häser, M.; Ahlrichs, R., Auxiliary basis sets to approximate Coulomb potentials. *Chemical Physics Letters* **1995,** *240* (4), 283-290.

39. Eichkorn, K.; Weigend, F.; Treutler, O.; Ahlrichs, R., Auxiliary basis sets for main row atoms and transition metals and their use to approximate Coulomb potentials. *Theoretical Chemistry Accounts* **1997,** *97* (1), 119-124.

40. Von Arnim, M.; Ahlrichs, R., Performance of parallel TURBOMOLE for density functional calculations. *Journal of Computational Chemistry* **1998,** *19* (15), 1746-1757.

41. Klamt, A., Conductor-like Screening Model for Real Solvents: A New Approach to the Quantitative Calculation of Solvation Phenomena. *The Journal of Physical Chemistry* **1995,** *99* (7), 2224-2235.

42. Klamt, A.; Jonas, V.; Bürger, T.; Lohrenz, J. C. W., Refinement and Parametrization of COSMO-RS. *The Journal of Physical Chemistry A* **1998,** *102* (26), 5074-5085.

43. Saleheen, M.; Heyden, A., Liquid-Phase Modeling in Heterogeneous Catalysis. *ACS Catalysis* **2018,** *8* (3), 2188-2194.

44. Faheem, M.; Suthirakun, S.; Heyden, A., New Implicit Solvation Scheme for Solid Surfaces. *The Journal of Physical Chemistry C* **2012,** *116* (42), 22458-22462.

45. Saleheen, M.; Verma, A. M.; Mamun, O.; Lu, J.; Heyden, A., Investigation of solvent effects on the hydrodeoxygenation of guaiacol over Ru catalysts. *Catalysis Science & Technology* **2019**.

46. Tshepelevitsh, S.; Oss, M.; Pung, A.; Leito, I., Evaluating the COSMO-RS Method for Modeling Hydrogen Bonding in Solution. *ChemPhysChem* **2013,** *14* (9), 1909-1919.

47. Zare, M.; Solomon, R. V.; Yang, W.; Yonge, A.; Heyden, A., Theoretical Investigation of Solvent Effects on the Hydrodeoxygenation of Propionic Acid over a Ni(111) Catalyst Model. *The Journal of Physical Chemistry C* **2020,** *124* (30), 16488-16500.

48. Saleheen, M.; Zare, M.; Faheem, M.; Heyden, A., Computational Investigation of Aqueous Phase Effects on the Dehydrogenation and Dehydroxylation of Polyols over Pt(111). *The Journal of Physical Chemistry C* **2019,** *123* (31), 19052-19065.

49. Marsh, K. N., COSMO-RS from Quantum Chemistry to Fluid Phase Thermodynamics and Drug Design. By A. Klamt. Elsevier: Amsterdam, The Netherlands, 2005. 246 pp. $US 165. ISBN 0-444-51994-7. *Journal of Chemical & Engineering Data* **2006,** *51* (4), 1480-1480.

50. Smith, J. M.; Ness, H. C. V.; Abbott, M. M., *Introduction to Chemical Engineering Thermodynamics*. McGraw-Hill: New York, 2005.

51. Grabow, L.; Hvolbæk, B.; Nørskov, J., Understanding Trends in Catalytic Activity: The Effect of Adsorbate–Adsorbate Interactions for CO Oxidation Over Transition Metals. *Topics in Catalysis* **2010,** *53*, 298-310.

52. Campbell, C. T., Future Directions and Industrial Perspectives Micro- and macro-kinetics: Their relationship in heterogeneous catalysis. *Topics in Catalysis* **1994,** *1* (3), 353-366.

53. Campbell, C. T., Finding the Rate-Determining Step in a Mechanism: Comparing DeDonder Relations with the “Degree of Rate Control”. *Journal of Catalysis* **2001,** *204* (2), 520-524.

54. Stegelmann, C.; Andreasen, A.; Campbell, C. T., Degree of Rate Control: How Much the Energies of Intermediates and Transition States Control Rates. *Journal of the American Chemical Society* **2009,** *131* (23), 8077-8082.

55. Akinola, J., Barth, I., Goldsmith, B. R., & Singh, N., Adsorption energies of oxygenated aromatics and organics on rhodium and platinum in aqueous phase. *ACS Catalysis*, **2020**, *10*(9), 4929-4941.

56. Sturm, J. M., Lee, C. J., & Bijkerk, F., Reactions of ethanol on Ru (0001). *Surface science*, **2013**, *612*, 42-47.

57. Avanesian, T., Gusmão, G. S., Christopher, P., Mechanism of CO2 reduction by H2 on Ru (0 0 0 1) and general selectivity descriptors for late-transition metal catalysts. *Journal of Catalysis*, **2016**, *343*, 86-96.

58. Sutton, J. E., Guo, W., Katsoulakis, M. A., & Vlachos, D. G., Effects of correlated parameters and uncertainty in electronic-structure-based chemical kinetic modelling. *Nature chemistry*, **2016**, *8*(4), 331.

59. Li, Q., García-Muelas, R., & López, N., Microkinetics of alcohol reforming for H_2 production from a FAIR density functional theory database. *Nature communications*, **2018**, *9*(1), 1-8.